energies

MDPI

Article

Optimal Configuration Model for Large Capacity Synchronous Condenser Considering Transient Voltage Stability in Multiple UHV DC Receiving End Grids

Lang Zhao [1,2], Zhidong Wang [1], Hao Sheng [2,*], Yizheng Li [1], Xueying Wang [1], Yao Wang [3] and Haifeng Yu [4]

[1] State Grid Economic and Technological Research Institute Co., Ltd., Beijing 102209, China; zhaolang@chinasperi.sgcc.com.cn (L.Z.); wangzhidong@chinasperi.sgcc.com.cn (Z.W.); liyizheng@chinasperi.sgcc.com.cn (Y.L.); wangxueying@chinasperi.sgcc.com.cn (X.W.)
[2] Key Laboratory of Smart Grid of Ministry of Education, Tianjin University, Tianjin 300072, China
[3] Economic and Technological Research Institute of State Grid Shanxi Electric Power Co., Ltd., Taiyuan 030021, China; wangyao@chinasperi.sgcc.com.cn
[4] Economic and Technological Research Institute of State Grid Hunan Electric Power Co., Ltd., Changsha 030021, China; yuhaifeng@chinasperi.sgcc.com.cn
* Correspondence: hao.sheng@tju.edu.cn; Tel.: +86-18001247807

Abstract: In a multi-fed DC environment, the UHV DC recipient grid faces significant challenges related to DC phase shift failure and voltage instability due to the high AC/DC coupling strength and low system inertia level. While the new large-capacity synchronous condensers (SCs) can provide effective transient reactive power support, the associated investment and operation costs are high. Therefore, it is valuable to investigate the optimization of SC configuration at key nodes in the recipient grid in a scientific and rational manner. This study begins by qualitatively and quantitatively analyzing the dynamic characteristics of DC reactive power and induction motors under AC faults. The sub-transient and transient reactive power output model is established to describe the SC output characteristics, elucidating the coupling relationship between the SC's reactive power output and the DC reactive power demand at different time scales. Subsequently, a critical stabilized voltage index for dynamic loads is defined, and the SC's reactive power compensation target is quantitatively calculated across different time scales, revealing the impact of transient changes in DC reactive power on the transient voltage stability of the multi-fed DC environment with dynamic load integration. Finally, an optimal configuration model for the large-capacity SC is proposed under the critical stability constraint of dynamic loads to maximize the SC's reactive power support capability at the lowest economic cost. The proposed model is validated in a multi-fed DC area, demonstrating that the optimal configuration scheme effectively addresses issues related to DC phase shift failures and voltage instability resulting from AC bus voltage drops.

Keywords: AC/DC hybrid grid; multi-feed DC; transient voltage stability; synchronous condenser; optimal configuration; dynamic load

check for updates

Citation: Zhao, L.; Wang, Z.; Sheng, H.; Li, Y.; Wang, X.; Wang, Y.; Yu, H. Optimal Configuration Model for Large Capacity Synchronous Condenser Considering Transient Voltage Stability in Multiple UHV DC Receiving End Grids. *Energies* **2024**, *17*, 5346. https://doi.org/10.3390/en17215346

Academic Editor: Claus Leth Bak

Received: 30 September 2024
Revised: 14 October 2024
Accepted: 25 October 2024
Published: 27 October 2024

Copyright: © 2024 by the authors. Licensee MDPI, Basel, Switzerland. This article is an open access article distributed under the terms and conditions of the Creative Commons Attribution (CC BY) license (https://creativecommons.org/licenses/by/4.0/).

1. Introduction

1.1. Research Background

In the context of the carbon peak and carbon neutrality strategy, the large-scale development and utilization of renewable energy (RE) have become crucial measures for transforming China's energy structure. Through the UHV DC grid, substantial RE can be transmitted to load centers in South China. However, with the continuous expansion and development of the load center AC grid, the increased feed into the DC environment at the receiving end, coupled with high AC/DC coupling strength, leads to low system inertia. The UHV DC faces significant challenges such as DC commutation failure and bipolar blocking, which introduce complexity and uncertainty to economic scheduling [1–3]. If the

system reactive power reserve is insufficient, it may even trigger a chain fault of multiple DC phase change failures. In addition, the increasing proportion of RE installed and dynamic load access in the recipient grid and the decreasing level of system inertia leading to post-fault voltage destabilization are also becoming more and more prominent [4,5].

Currently, the mainstream reactive power compensation devices are SVC, STATCOM and SC. Although SVC, STATCOM and other electronic reactive power compensation are controllable, there are problems such as small capacity, high loss, and high failure rate [6–8]. The new self-developed SC has a large capacity, strong reactive power support ability, and has the advantage of not being limited by the bus voltage [9]. In addition, it can respond to the bus voltage change in milliseconds after a fault and has a short-term reactive power overload capacity 2–3 times the normal level, which can effectively solve the problem of DC phase shift failure and voltage instability caused by the drop of the AC bus voltage [10].

1.2. Literature Survey

The feasibility of overload capabilities for large-capacity SCs in addressing transient dynamic reactive power shortages in the receiving end grid within a "strong direct and weak cross" hybrid grid was analyzed in [11]. The fault transient reactive power of UHV AC/DC hybrid grids after the integration of SCs was examined in [12], where it was demonstrated that the short-term overload capacity of the SC could effectively enhance transient bus voltage post-fault. However, an analysis of DC reactive power changes at different stages was not conducted, leading to significant errors in the sub-transient stage results. Due to the high initial investment and operation and maintenance costs of large-capacity SCs [13], the optimal configuration of the SC in a multi-feeder DC environment must be studied scientifically and reasonably to ensure stability of the receiving end voltage at minimal economic cost.

Research on the optimal configuration of large-capacity SCs had primarily been focused on the UHV DC sending end configuration, with fewer studies conducted on the receiver configuration. The DC blocking transient overvoltage constraints were considered, and collaborative planning of the SC and SVC at the transfer station at the sending end of a large energy base was proposed in [14]. The capacity of large-capacity and distributed SCs was optimized in [15] with the objectives of sending end voltage stability and maximum consumption capacity. Weak links in RE clusters were identified in [16] based on short circuit ratio calculations of each plant station in new energy bases, targeting reactive power compensation equipment. The literature mentioned above mainly aimed to inhibit overvoltage in wind power generation, overvoltage caused by DC blocking, and enhance RE consumption capacity and sending end voltage stability in the sender SC configuration [17]. In contrast to the weak in-phase reactive power regulation of the sending end SC, a significant impact on the strength of the AC system was caused by the configuration of the SCs at the receiving end. Unlike the sending end, numerous reactive dynamic loads were present at the receiving end, leading to a more serious transient voltage stability problem [18]. The prevention of DC phase change failure and an optimal configuration method for the receiving end SC under investment cost constraints were the focus of the study developed in [19]. However, a comprehensive analysis of the DC transient reactive power behavior in different time scales after a fault was not provided, nor was the impact of the SC's reactive power compensation on bus voltage stability under various transient conditions clarified. In [20,21], the transient voltage drop area under phase change failure was analyzed based on the multi-feed-in DC interaction factor to determine the optimal placement location of the SC. However, the change in reactive power output of the SC in different transient time scales and the impact of large-scale dynamic load integration at the receiving end on transient voltage stability were not considered.

1.3. Research Focus and Organization

Therefore, this study focuses on the large-capacity SC configuration considering transient voltage stabilization under a multi-feed-in DC environment. However, based on the literature survey, there are some limitations of the current study. They are as follows:

(1) The analysis of reactive power demand in the DC system and the reactive power output of the SC in different transient stages following a fault lacked depth and failed to analyze the coupling relationship across different time scales;
(2) The impact of the increasing proportion of dynamic loads, such as induction motors, on transient voltage stability at the receiving end with multiple DC feeders was not taken into consideration;
(3) Existing research primarily focused on configuring the SC at the receiving end based on phase change failure. However, phase change failure alone did not fully and accurately reflect the voltage stability level at the receiving end of an AC/DC hybrid system.

Therefore, this study begins by qualitatively and quantitatively analyzing the dynamic characteristics of DC reactive power and induction motors under AC faults. The sub-transient and transient reactive power output model is established to describe the SC output characteristics, elucidating the coupling relationship between the SC's reactive power output and the DC reactive power demand at different time scales. Subsequently, a critical stabilized voltage index for dynamic loads is defined, and the SC's reactive power compensation target is quantitatively calculated across different time scales, revealing the impact of transient changes in DC reactive power on the transient voltage stability of the multi-fed DC environment with dynamic load integration. Finally, an optimal configuration model for the large-capacity SC is proposed under the critical stability constraint of dynamic loads to maximize the SC's reactive power support capability at the lowest economic cost.

The article is organized as follows. In Section 2, the reactive power changes in the converter and DC system in each transient stage after an AC fault and their impact on the transient voltage stability at the receiving end are analyzed based on the dynamic load reactive power characteristics. In Section 3, sub-transient and transient reactive power output models are established to describe the SC output characteristics, elucidating the coupling relationship between the SC's reactive power output and the DC reactive power demand at different time scales. In Section 4, a critical stabilized voltage index for dynamic loads is defined, and the SC's reactive power compensation target is quantitatively calculated across different time scales. An optimal configuration model for the large-capacity SC is proposed under the critical stability constraint of dynamic loads to maximize the SC's reactive power support capability at the lowest economic cost. Finally, the proposed model is validated in Section 5. Finally, the conclusion and limitation analysis of the article is arranged in Section 6.

2. Transient Voltage Stability Analysis of UHV AC/DC Hybrid Grid at Receiving End

Unlike the off-grid risk associated with RE units in sending end grids, the receiving end of the UHV AC/DC hybrid grid contains substantial reactive dynamic loads. Ensuring the transient voltage stability of the receiving end under multi-feeding DC conditions is crucial. This section examines the reactive power variations of the converter and DC system during each transient phase following an AC fault and analyzes their impact on the transient voltage stability of the receiving end, based on the reactive power characteristics of dynamic loads.

2.1. Transient Reactive Power Demand of the Converter Considering Phase Change Failure

As a key component in the AC/DC hybrid grid, the converter consumes a significant amount of reactive power during phase change states. Consequently, converter stations

are equipped with numerous reactive power compensation devices. The reactive power exchange $Q_{ac\text{-}dc}$ in the AC/DC hybrid system is expressed as follows:

$$Q_{ac-dc} = Q_{rpc} - nQ_{inc} \tag{1}$$

where Q_{rpc} represents the reactive power provided by the SVC of the converter station. Q_{inc} represents the reactive power consumed by a single six-pulse wave converter. n represents the number of six-pulse wave converters.

To analyze the transient reactive power changes of the UHV DC system after an AC fault, the reactive power demand of the DC converter can be formulated as follows:

$$U_d = \frac{3\sqrt{2}}{\pi} U_s \cos\gamma - \frac{3}{\pi} X_c I_d \tag{2}$$

$$Q_{inc} = U_d I_d \tan(\gamma + \mu/2) \tag{3}$$

$$\cos\gamma = \cos\alpha + \frac{\sqrt{2}}{U_s} X_c I_d \tag{4}$$

$$\alpha + \gamma + \mu = \pi \tag{5}$$

where U_d and I_d represent the real-time voltage and current of the UHV DC system, respectively. X_c represents the equivalent reactance of the converter. α, μ, and γ represent the trigger angle, overlap angle, and turn-off angle of the converter, respectively.

The reactive power demand of the converter is influenced by the operating conditions of the DC system after a fault and control strategies during different transient phases. This paper classifies and analyzes whether DC phase change failure occurs after an AC fault. The Cigre test system simulates the transient conditions of an AC side grounding fault (fault time is 5 s, removal time is 0.5 s), where the bus voltage drops to 0.9 p.u. and 0.7 p.u., corresponding to two scenarios: DC without phase change failure (dc-1) and phase change failure (dc-2). The Cigre test system material can be found in [22] in detail. The DC current and reactive power consumption of the converter are shown in Figure 1 [22]. The DC control strategies for these conditions are shown in Table 1 [22].

Table 1. Control mode of DC sending and receiving end under two working conditions.

Whether Phase Change Failure or Not	Operational Status		Sending Side Control Strategy	Receiving Side Control Strategy
No phase change failure	Fault period	1	Low voltage current limit + constant current	Constant blocking angle
		2		Current deviation + constant blocking angle
		3		Constant blocking angle
	Recovery period	4		Current deviation + constant blocking angle
		5	Constant current	Constant blocking angle
Phase change failure	Fault period	1	Low voltage current limit + constant current	Current deviation + constant blocking angle
		2		Constant current
		3		Constant blocking angle
	Recovery period	4		Current deviation + constant blocking angle
		5	Constant current	Constant blocking angle

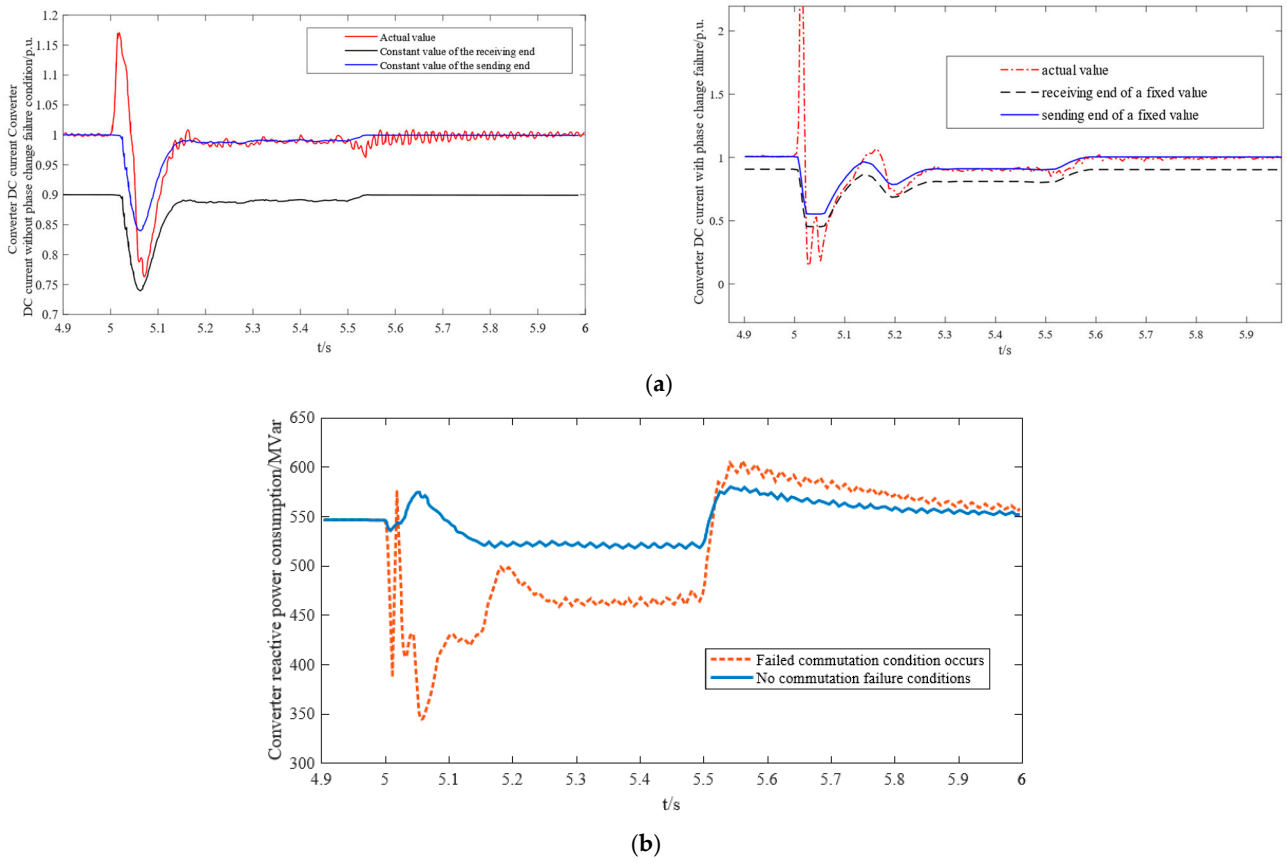


Figure 1. Comparison of DC current and reactive power consumption. (**a**) Comparison of DC currents under AC side grounding fault. (**b**) Comparison of reactive power consumption under AC side grounding fault.

A qualitative analysis of the scenario without phase change failure reveals that, due to the constant current control strategy at the sending end, the DC current I_{dc} of Stage 1 drops rapidly from the fault current at the fault's onset. Additionally, due to the low-voltage current limiting control strategy, I_{dc} will be lower than the sender-side constant value. At this time, the current deviation effect increases the blocking angle γ, causing the reactive power demand Q_{inc} of the converter to rise gradually. In Stage 2, as I_{dc} approaches the end-of-feed trimming value, the blocking angle γ decreases gradually to the fault steady-state value, resulting in a gradual reduction in Q_{inc}. In Stage 3, at the fault steady state, the receiving end reverts to the constant blocking angle (fault steady-state value) control. Because the DC voltage is lower than the normal value, Q_{inc} is slightly reduced at the fault steady state. In Stage 4, the instant of fault removal causes Q_{inc} to increase instantaneously as the blocking angle remains at the fault steady-state value. In Stage 5, the current bias effect reduces the blocking angle γ. Due to the low-voltage current limiting strategy at the sending end, the DC current recovery speed is restricted, causing a slow return to the pre-fault steady-state value.

The transient process of the DC current during a phase change failure is qualitatively analyzed. In Stage 1, the phase change failure induces Id fluctuations due to a short circuit, leading to significant Q_{inc} variations. As shown in Figure 1a, these fluctuations in I_d, being less than the integrated values at both the sender and receiver ends, cause current deviations. These deviations, under the combined actions of shut-off angle control and fixed current control, initiate corrective responses. During this pre-competitive process, the receiving end continues to experience current deviations controlled by the shut-off angle. An increase in γ results in increased I_{dc} and Q_{inc}, while an increase in Id reduces the current deviation, causing γ to decrease along with I_{dc} and Q_{inc}. This continues until the fluctuating

I_d and fixed current deviation are minimized, allowing fixed current control at the sending end to dominate, at which point Q_{inc} reaches its minimum. In Stage 2, both the sending and receiving ends operate in constant current control mode, causing I_{dc} and Q_{inc} to rise slowly. In Stage 3, Q_{inc} reaches its maximum value during the fault phase, enters a fault steady state, and reverts to constant blocking angle (fault steady-state value) control. Subsequent stages mirror the conditions of non-phase-change failure and will not be detailed here. The $Q_{ac\text{-}dc}$ waveform of reactive power exchange in the AC/DC hybrid system under both conditions is illustrated in Figure 2 [22].

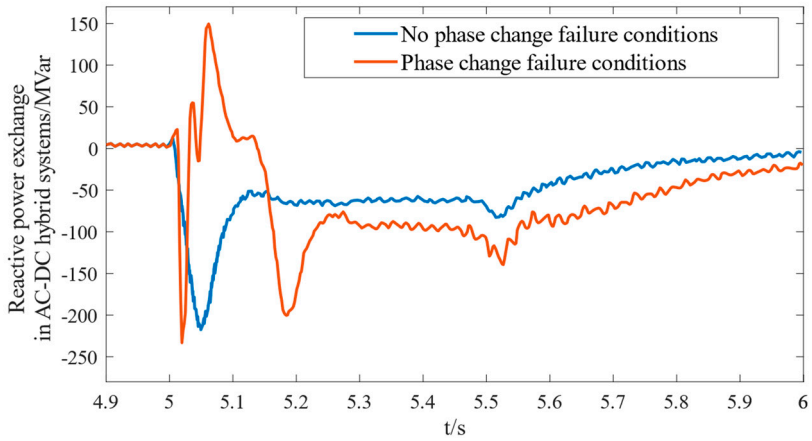


Figure 2. Reactive power exchange in AC/DC hybrid systems.

It is observed that, during a phase change failure, both Q_{rpc} and Q_{inc} decrease instantaneously, with Q_{rpc} experiencing a smaller decrease than Q_{inc}, leading to an immediate increase in $Q_{ac\text{-}dc}$. Regardless of phase change failure, a substantial amount of reactive power is absorbed during the transition from transient to steady state. The system continues to absorb reactive power for an extended period post-fault. Reactive power Q_{rpc} provided by reactive power compensation equipment (SVC) is proportional to the square of its bus voltage. During an AC system fault, reduced bus voltage significantly diminishes the output of the reactive power compensation equipment. This transient reactive power change opposes the system's demand, necessitating the urgent supplementation of reactive power sources, such as regulators, to restore transient voltage stability.

2.2. Transient Reactive Power Demand Analysis for Dynamic Loads Based on Power-Slip Curve

Dynamic loads, represented by induction motors, are one of the triggers for voltage instability in the UHV AC/DC hybrid system. The topology of the UHV AC/DC hybrid grid considering dynamic loads is shown in Figure 3. In this section, the transient reactive power demand of dynamic loads is analyzed based on the power-slip curve.

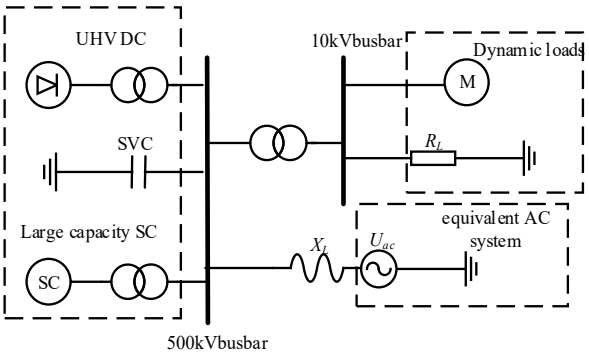


Figure 3. UHV AC/DC hybrid grid topology considering dynamic loads.

First, the UHV AC/DC hybrid system is subjected to the Davignan circuit equivalent, as shown in Figure 4.

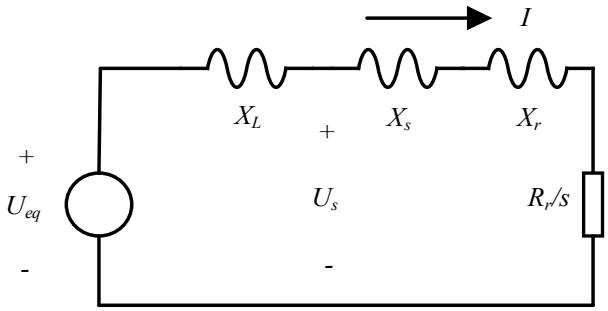


Figure 4. Equivalent circuits for ultra-high voltage AC/DC hybrid grids.

U_{eq} is the equivalent AC power source. X_L is the equivalent reactance of the AC/DC interconnection. U_s is the terminal voltage. X_s, X_r, R_r, and s are the stator reactance, rotor reactance, rotor resistance, and slip of dynamic loads, respectively. P_{dc} and Q_{dc} are the DC active and reactive power.

During the transition from transient to steady state after an AC fault, the reactive power demand increases, while changes in active power can be ignored. Additionally, the effect of active power on the bus voltage is negligible ($U_{ac} \approx U_s$). Therefore, the equivalent power supply U_{eq} and electromagnetic torque P_e can be simplified and expressed as follows:

$$U_{eq} = X_L U_{ac}\left(\frac{1}{X_L} + \frac{Q_{dc}}{U_{ac}^2}\right) \tag{6}$$

$$P_e = \frac{R_r\left(U_{ac} + \frac{Q_{dc}}{U_{ac}+S_{ac}}\right)^2}{\left(X_s + X_r + \frac{S_M}{S_{ac}}\right)^2 s + R^2{}_r/s} \tag{7}$$

where S_{ac} and S_M represent the AC system short-circuit capacity and dynamic load capacity, respectively. Additionally, the mechanical power of the induction motor is shown as follows:

$$P_k = \Omega k_L\left[a + (1-a)(1-s)^2\right] \tag{8}$$

where Ω represents the mechanical angular velocity of rotation. k_L represents the loading rate of dynamic load, and a represents the mechanical torque. The power-slip waveform for different operating conditions is shown in Figure 5.

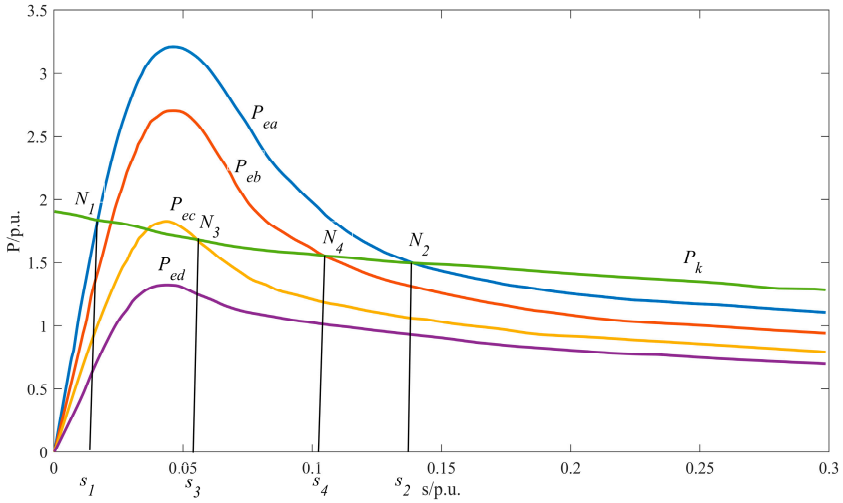


Figure 5. Power-slip waveform under different conditions.

Under the rated conditions, the dynamic load represented by the induction motor operates at point N_1 of the P_{ea} curve and will return to point N_1 after a small disturbance. However, if the slip exceeds s_2 due to a serious system failure, the motor will continue to decelerate until it reaches a blocked rotation.

When an AC fault occurs, the bus voltage drops. At this time, two scenarios may occur, as shown in the curves P_{ec} and P_{ed}. If the electromagnetic power after the fault follows curve P_{ec}, the system will not destabilize as long as the slip reaches s_3 before the fault is cleared. However, a serious system failure causes the electromagnetic power to fall to curve P_{ed}, which does not intersect with P_k. As the mechanical power remains greater than the electromagnetic power, the rotor deceleration increases slip until the motor blocks, leading to system voltage destabilization.

Furthermore, after the removal of the AC system fault, there will be a certain amount of reactive power consumption during the DC recovery period, causing the bus voltage to be lower than the rated voltage for a period of time. The electromagnetic curve during this period is shown in P_{eb}. The corresponding critical stable operation point will shift from N_2 at rated conditions to N_4. Therefore, the reactive power absorption of the converter during the fault recovery period increases the risk of system voltage destabilization.

3. Reactive Power Output of Large-Capacity SC Coupled with DC Reactive Power Demand Under Different Time Scales

3.1. Reactive Power Output Model of Large-Capacity SC in Sub-Transient and Transient Phase of Multi-Feed DC Environment

Similar to a synchronous motor, the SC power can be expressed as follows:

$$\begin{cases} P_{SC} = u_d i_d + u_q i_q \approx \frac{E_q U_d}{X_d} \sin\delta \approx 0 \\ Q_{SC} = u_q i_d - u_d i_q \approx u_q i_d \approx U_s i_d \end{cases} \tag{9}$$

When excitation regulation is not considered, the voltage drop of the SC after a system short circuit is given by $\Delta u_d = u_d - u_{d0}$, $\Delta u_q = u_q - u_{q0} \approx U_{s1} - U_{s0}$.

$$\begin{cases} \psi_d = -\Delta u_d = p\psi_d - \psi_q - r i_d \\ \psi_q = -\Delta u_q = p\psi_q - \psi_d - r i_q \end{cases} \tag{10}$$

Its time-domain expression after the Laplace inverse transform and superposition of the steady-state components is as follows:

$$\Delta i_d = -\Delta U_s \begin{bmatrix} \left(\frac{1}{X_d''} - \frac{1}{X_d'}\right) e^{-\frac{t}{T_d''}} + \left(\frac{1}{X_d'} - \frac{1}{X_d}\right) e^{-\frac{t}{T_d'}} \\ -\frac{\cos(\omega t+\delta)}{X_d''} e^{-\frac{t}{T_a}} + \frac{1}{X_d} \end{bmatrix} \tag{11}$$

$$Q''_{SC} = U_{s1}(U_{s0} - U_{s1}) \begin{bmatrix} \left(\frac{1}{X_d''} - \frac{1}{X_d'}\right) e^{-\frac{t}{T_d''}} + \left(\frac{1}{X_d'} - \frac{1}{X_d}\right) e^{-\frac{t}{T_d'}} \\ -\frac{\cos(\omega t+\delta)}{X_d''} e^{-\frac{t}{T_a}} + \frac{1}{X_d} \end{bmatrix} \tag{12}$$

It can be seen that the large-capacity SC output at the sub-transient stage includes the AC component decaying with T_a as a constant, the steady-state component, the sub-transient component caused by the damping winding decaying with T_d'' as a constant, and the transient component caused by the excitation winding decaying with T_d' as a constant. Unlike the reactive power output of the SVC, the sub-transient process output of the SC is proportional to the bus voltage drop. The larger the bus voltage drop, the larger the

sub-transient output of the SC, effectively preventing voltage instability and avoiding DC phase change failure. The inertia link of its excitation system is expressed as follows:

$$\Delta E_f = \frac{K_a \Delta U_s}{1 + Ts} \tag{13}$$

$$E'_q = U_s + X'_d i_d \tag{14}$$

$$T'_d \frac{dE'_q}{dt} = E_f - E'_q - (X_d - X'_d) i_d \tag{15}$$

Substituting (13) into (14) and (15) and performing the Laplace inverse transform, the Δi_d time-domain expression is as follows:

$$\Delta i_d = -\Delta U_s \frac{1}{X'_d} + \Delta U_s \otimes \left(\frac{K_a - 1}{X_d} + \frac{1}{X'_d} \right) \left(1 - e^{\frac{-X_d t}{X'_d T'_d}} \right) \tag{16}$$

where $\otimes$ represents the convolution.

$$Q'_{SC} = U_{s1} \left\{ \begin{array}{l} (U_{s0} - U_{s1}) \otimes \left(\frac{K_a - 1}{X_d} + \frac{1}{X'_d} \right) \left(1 - e^{\frac{-X_d t}{X'_d T'_d}} \right) \\ -(U_{s0} - U_{s1}) \frac{1}{X'_d} \end{array} \right\} \tag{17}$$

The strong excitation control of the excitation system will increase the reactive power output of the SC.

3.2. Coupling Relationship Analysis Between Reactive Power Output of Large-Capacity SC and DC Reactive Power Demand Under Different Time Scales

The coupling relationship between the SC reactive power output and DC reactive power demand is analyzed for the sub-transient and transient processes following an AC fault in the UHV AC/DC hybrid system, as well as the recovery process after fault removal.

(1) Sub-transient Process after AC System Fault (Stage 1):

The DC system (converter) needs to consume reactive power to transition to the transient stage. As shown in Figure 1b, under the unchanged phase fault condition, the converter's reactive power demand increases slightly. At this time, the SC's output is positively correlated with the degree of bus voltage drop, effectively meeting its reactive power demand. In the phase change fault condition, the converter's reactive power demand fluctuates and then decreases. At this point, the instantaneous drop of Q_{rpc} is smaller than that of Q_{inc}, and $Q_{ac\text{-}dc}$ increases instantaneously. The SC and SVC reactive power compensation ensures that the converter remains stable in the sub-transient state.

(2) Transient Process after AC System Fault:

In the case of a non-phase-change fault, the transient phase output Q'_{SC} is greater than the sub-transient phase output Q''_{SC}. The reactive power demand of the DC system decreases in the transient phase. Therefore, as long as the sub-transient phase reactive power consumption is satisfied, it ensures that the voltage remains stable in the transient phase. Under the phase change fault condition, as shown at point M in Figure 1b, the DC system reactive power demand reaches its maximum at this stage. The SC's reactive power output peaks under strong excitation in the initial stage of the transient phase. To theoretically avoid system voltage instability, it must satisfy $nQ'_{SC} \geq Q_{dcmax}$ (where n is the number of SC configurations). However, if the fault is severe, it can lead to the system voltage dropping below the dynamic load critical stabilization voltage U_k (as shown in Figure 5 P_{ed}), resulting in induction motor blocking and system instability. Therefore, the SC must ensure sufficient dynamic reactive power compensation to maintain bus voltage U_s above the dynamic load critical stabilization voltage U_k across all time scales.

(3) Recovery Process after Fault Removal:

Given that the transient time constant of the large-capacity SC is $T'_d \approx 7.5$ s, it can continue to output reactive power for an extended period under strong excitation, accelerating bus voltage recovery.

4. Optimal Configuration Model of Large-Capacity SC Considering Transient Voltage Stability in Multi-Fed DC Environment

4.1. Objective Function of Optimal Regulator Configuration in Multi-Feeder DC Areas Considering Economic Cost and Transient Voltage Stability

The installation location and capacity of different SCs significantly affect their strength. This study aims to optimize the configuration of the SC in multi-feeder DC areas by maximizing the reactive power support capability of the SC while minimizing economic costs. The economic cost sub-objective function for the large-capacity SC is expressed as follows:

$$\min f_1 = \frac{r\left[\sum_{i=1}^{n} C_{ta,i} + C_m Q_i\right](1+r)^L}{n[(1+r)^L - 1]} \tag{18}$$

where $C_{ta,i}$ represents the installation cost of the SC at converter station i. C_m represents the operation cost. Q_i represents the SC installed capacity at converter station i. n represents all installation points of the SC. L represents the service life of the SC. r represents the discount rate. This study uses the system transient voltage stability margin index λ for quantitative calculation. The dynamic load critical stability voltage U_k is the minimum voltage threshold that prevents system destabilization across multiple time scales following an AC system fault. Thus, the sub-objective function for maximizing system reactive power support can be expressed as follows:

$$\begin{aligned} &\max f_2 = \sum_{i=1}^{n} \lambda_i \\ &\lambda_i = \int_{t_0}^{t_1} (U_{it} - U_{ik})dt + \int_{t_1}^{t_2} (U_{it} - U_{ik})dt + \int_{t_2}^{t_3} (U_{it} - U_{ik})dt \end{aligned} \tag{19}$$

where λ_i represents the transient voltage stability margin. The time scales $t_0 - t_1$, $t_1 - t_2$, and $t_2 - t_3$ represent the transient phase, transition phase, and recovery phase after fault removal, respectively. U_{it} represents the bus voltage at moment t of converter station i. U_{ik} represents the critical stabilization voltage of the bus at converter station i. The solution method is detailed in Section 4.2.

The economic cost sub-objective function and the reactive capacity support sub-objective function are not solved with the same magnitude. Therefore, it is impossible to directly multiply the economic cost and reactive power support to solve these functions. The traditional method will inevitably use subjective assignment, which will result in the lack of fairness of the results. The traditional linear weighting method often involves subjective assignments, leading to potential bias in the results. This study transforms the multi-objective problem by minimizing the Euclidean distance as follows:

$$\min F = \sqrt{\left[\frac{f_1(x) - f_1^*}{f_1^*}\right]^2 + \left[\frac{f_2(x) - f_2^*}{f_2^*}\right]^2} \quad x \in M \tag{20}$$

where x represents different configuration schemes of the SC. M represents the solution set comprising all possible configuration schemes. f_1^* and f_2^* represent the optimal solutions of individual sub-objective functions within the solution set M.

4.2. Reactive Power Compensation Constraints in Multi-Feeder DC Areas Considering Dynamic Load Critical Voltage Stability

4.2.1. Dynamic Load Critical Stability Voltage Solution Methods

To prevent system voltage collapse due to the large-scale blocking caused by the electromagnetic torque deficiency of induction motors in the event of UHV AC/DC hybrid

system failure, it is essential to ensure stable voltage at each converter station during faults. Specifically, the bus voltage of each converter station must exceed the dynamic load critical stabilization voltage U_k at the time of fault. The critical stabilization voltage U_{ik} at converter station i is calculated as follows.

When the AC system experiences a severe fault, in the critical steady state (when the slip is s_3), the mechanical torque equals the electromagnetic torque.

$$\begin{aligned} T_k &= \frac{P_k}{\Omega} = k_L[a + (1-a)(1-s)^2] \\ T_p &= \frac{P_e}{\Omega} == \frac{R_r(U_{ik})^2}{\Omega(X_s + X_r + \frac{S_M}{S_{ac}})^2 s + R^2{}_r/s} \end{aligned} \tag{21}$$

Additionally, during the transition from rated condition to critical condition, with slip moving from s_1 to s_3, the rotor motion equation must also be satisfied, as follows:

$$\frac{t_k}{\Omega T_j} = \int_{s_1}^{s_3} \frac{1}{P_k - P_e} ds \tag{22}$$

where t_k represents the fault removal time. T_J represents the rotor inertia time constant. T_k and T_P represent the mechanical torque and electromagnetic torque, respectively. The critical steady-state slip s_3 and U_{ik} can be determined by linking Equations (21) and (22).

4.2.2. Reactive Power Compensation Constraints in Multi-Feeder DC Areas

(1) The reactive power compensation constraint for a single converter station can be derived as follows. Firstly, irrespective of the phase change failure, when the DC reactive power demand reaches its maximum, the DC current is governed by a low-voltage current-limiting control. Its value is approximated by the low-voltage current-limiting control current.

$$I_d \approx f_I(U_d) = \begin{cases} 1 & U_d > 0.9 p.u. \\ 0.9U_d + 0.18 & 0.4 p.u. \le U_d \le 0.9 p.u. \\ 0.55 & U_d \le 0.4 p.u. \end{cases} \tag{23}$$

where $f_I()$ represents the low-voltage current-limiting control model. Consequently, the maximum converter reactive power consumption $Q_{inc,max}$ at the fault's onset (stage 1) is as follows:

$$Q_{inc,\max} \approx \frac{6X_c[f_I(U_{ik})]^2}{\mu\pi} \cos\frac{\mu}{2} \tag{24}$$

Therefore, for converter station i, the reactive power compensated by the SVC or SC at the fault's onset must exceed the maximum converter reactive power consumption $Q_{inc,max}$.

$$Q_{ac-dc} + U_k^2/U_{s0}^2 Q_{SVC} + m_i \frac{U_{s0}^2 - U_{s0}U_k}{X'_d} > n_i Q_{inc,\max} \tag{25}$$

where $Q_{ac\text{-}dc}$ represents the reactive power exchange in the AC/DC hybrid system. Q_{SVC} represents the rated reactive power output. m_i and n_i represent the number of SCs and converters installed in converter station i.

(2) Multi-feeder DC area reactive power compensation constraints: for multi-feeder DC regions (multiple converter stations), the reactive power supplied by their access SCs must be maintained to prevent system destabilization during transient processes.

$$\sum_{i=1}^{n} m_i \frac{U_{s0}^2 - U_{s0}U_k}{X'_d} > \sum_{i=1}^{n} n_i Q_{inc,\max} \tag{26}$$

(3) Bus voltage stabilization constraints: the following constraints are set according to the State Grid and Southern Grid transient voltage technical specifications [23,24]:

$$\begin{aligned} U_{i(t_0+1)} &> 0.75U_{is0} \\ U_{i(t_0+10)} &> 0.8U_{is0} \\ U_{i(t_0+60)} &> 0.9U_{is0} \end{aligned} \tag{27}$$

In addition to meeting the above constraints, this model also includes the investment cost constraints of the regulator, the installation capacity constraints of the regulator, and the operational constraints of the UHV AC/DC hybrid grid, which are not detailed here.

4.3. Solving Process of the SC Optimal Configuration Model Under Multi-Feeder DC Environment

For transient simulation of the more complex UHV AC/DC hybrid system, DIGSILENT 2021 simulation software is used to simulate AC faults under multi-feeder DC conditions, and the Matlab 2021a particle swarm optimization algorithm is employed to solve the optimal configuration of large-capacity regulators [25]. The solution steps are shown in Figure 6 and are as follows:

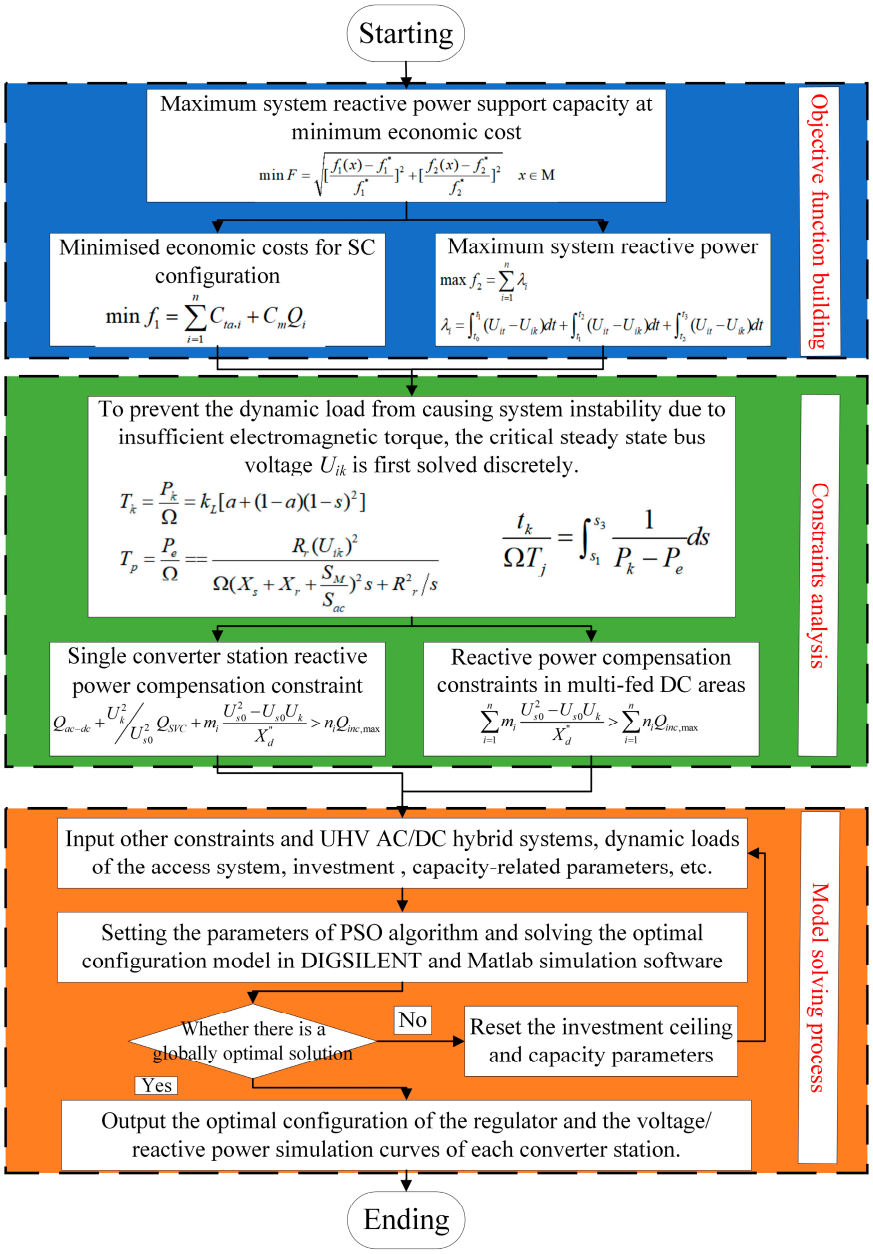


Figure 6. Solving process of the optimal configuration model.

(1) Establish the optimal configuration model of the SC with the objective of achieving the maximum reactive power support capability of the synchronous regulator to the system with the least economic cost;

(2) Establish the constraints of reactive power compensation in single converter station and multi-feeder DC area;

(3) Input other constraints and UHV AC/DC hybrid systems, dynamic loads of the access system, investment, capacity-related parameters, etc.;

(4) Set the parameters of the PSO algorithm and solve the optimal configuration model in DIGSILENT and Matlab simulation software;

(5) Judge whether there is a globally optimal solution;

(6) If there is not a globally optimal solution, reset the investment ceiling and capacity parameters and return to step 3;

(7) If there is a globally optimal solution, output the optimal configuration of the regulator and the voltage/reactive power simulation curves of each converter station.

5. Case Study

5.1. Parameter Selection

The topology of a local grid with multiple feeds into a DC area is depicted in Figure 7. The UHV DC parameters, SC parameters, induction motor parameters, and dynamic load of each converter station are provided in Tables 2, 3, 4, and 5, respectively. The four converter stations serve as locations for deploying large-capacity SCs, and the SC capacity at each DC station is considered a variable to be optimized in [26]. The AC lines described in this paper are all inter-provincial 500 kV lines. Their line lengths are within about 200–500 km. They are not listed because they are not within the specific research scope of this paper.

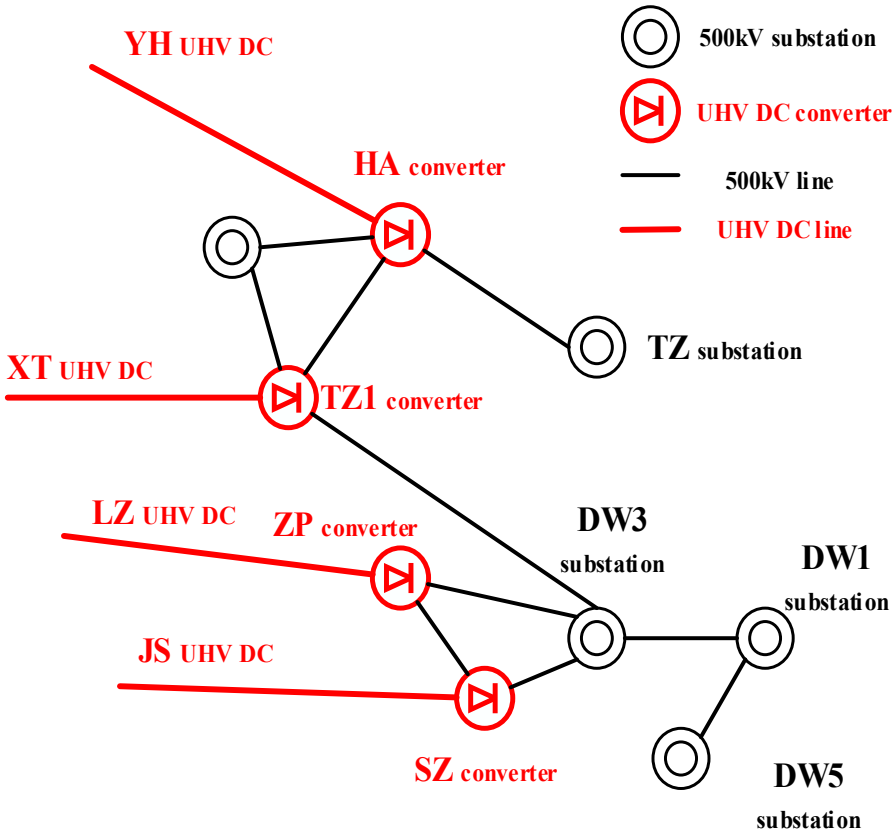


Figure 7. Wiring diagram of a multi-feed DC area in China.

Table 2. DC system parameters connected with 500 kV AC grid.

UHV DC Name	UHV DC Length	Rated Power	Rated Voltage	Short Circuit Ratio
JS	1150 km	7000 MW	±800 kV	2.52
XT	920 km	5000 MW	±800 kV	3.75
LZ	695 km	3500 MW	±500 kV	4.60
YH	1290 km	7500 MW	±800 kV	3.87

Table 3. The parameters for the 300 MVar SC.

Parameter	Value	Parameter	Value
Sub-transient reactance X''_d	10.9 p.u.	Transient reactance X'_d	16.1 p.u.
Sub-transient time constant T''_d	0.06 s	Transient time constant T'_d	7.47 s
Excitation system strong excitation multiplier	2.41	Stator non-periodic component time constant T_a	21.96 s

Table 4. The parameters for the induction motor.

Parameter	Value	Parameter	Value
Stator reactance X_s	0.301 p.u.	Steady-state slip s_1	0.013 p.u.
Rotor reactance X_r	0.024 p.u.	Rotor inertia time constant T_J	2.1 s
AC/DC interconnection equivalent reactance X_L	0.656 p.u.	Mechanical torque	0.155

Table 5. Dynamic load share of each converter station.

UHV Converter Name	DC Off-Grid Load	Constant Impedance Load Share	Dynamic Load Share
SZ	7000 MW	36.4%	63.6%
TJ1	5000 MW	47.1%	52.9%
HA	7500 MW	33.3%	66.7%
ZP	3500 MW	39.8%	60.2%

5.2. Optimal Configuration Results Analysis for SCs in a Multi-Feed DC Environment

According to DIgSILENT 2021 and Matlab simulation results, the sub-objective function values for all configuration schemes are calculated, and the two sub-function coupling relationships are illustrated in Figure 8.

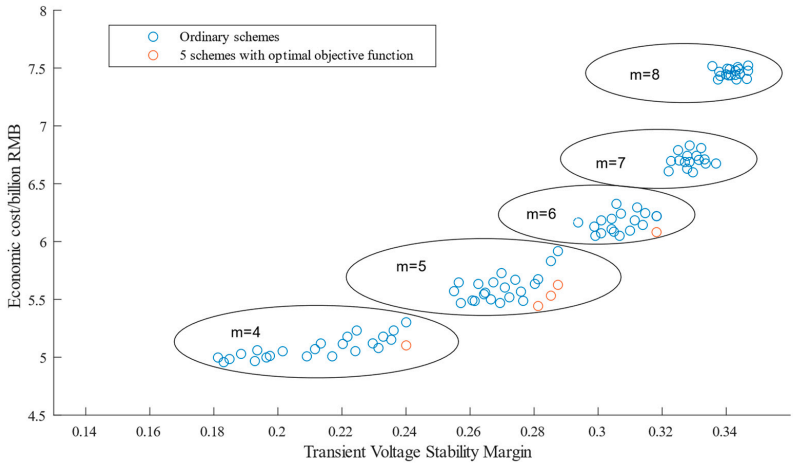


Figure 8. Sub-function coupling relationship.

It is evident that at least four SCs are required in the system to meet the transient stability requirements of the AC/DC hybrid system. It is impractical to excessively improve

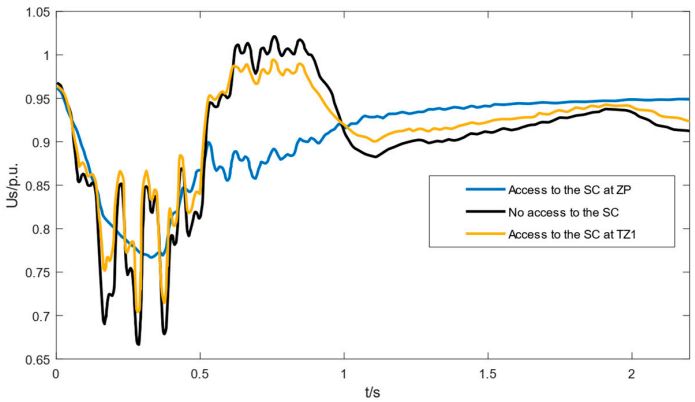
the transient voltage stability margin at a significant additional economic cost. Therefore, this paper aims to minimize the Euclidean distance, balancing economic benefits and transient voltage stability while ensuring safety. The five most-preferred schemes are shown in Table 6.

Table 6. Configuration results for the optimal 5 scenarios.

Numbers	Location and Capacity of SC Access (MVar)				Total Number of SC Access	Total Capacity of SC Access (MVar)	Total Economic Cost (Billion Yuan)	Transient Voltage Stability Margin	Objective Function Value F
	SZ	HA	ZP	TZ1					
Scheme 1	2	1	1	0	4	1200	0.51	0.24	0.367
Scheme 2	3	1	1	0	5	1500	0.55	0.284	0.355
Scheme 3	3	1	0	1	5	1500	0.56	0.287	0.358
Scheme 4	3	0	1	1	5	1500	0.57	0.289	0.361
Scheme 5	3	1	1	1	6	1800	0.6	0.316	0.372

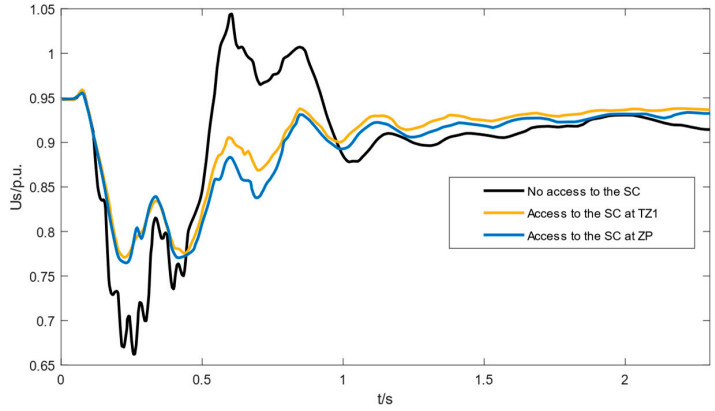
Scheme 2, with SZ access to 900 MVar, HA access to 300 MVar, and ZP access to 300 MVar, achieves the maximum system reactive power support capability of the SC at the lowest economic cost. Table 6 indicates that the SZ converter station has the highest demand for the SC. This is due to the poor transient voltage stability caused by the weak strength of the AC grid in the SZ area and the access to a large number of dynamic loads. Additionally, the close proximity between the SZ and ZP converter stations leads to a larger interaction factor, with SZ's transient voltage fluctuations significantly impacting ZP. Therefore, the SC at the SZ converter station should be prioritized over ZP once the upper limit is reached. To verify the optimal configuration, Scheme 2, Scheme 3 with the same capacity but different access locations, and the scheme without access to the SC (Scheme 6) are compared and analyzed. The ZP–DW3 line at the 40% position (A) and the TZ1–DW3 line at the 5% position (B) are set to experience a three-phase short-circuit fault to compare the transient voltage waveforms of ZP and TZ1, as shown in Figure 9.

As shown in Figure 9a, a fault at ZP–DW3 has the greatest impact on the ZP converter station. The voltage dips and recovery speeds of Scheme 2, which accesses the 300 MVar regulator at ZP, are significantly better than those of Schemes 3 and 6. The transient voltage waveforms in Scheme 6 indicate that after an AC system fault. The voltage dips and recovery speeds of Scheme 2, with the 300 MVar SC connected at ZP, are markedly better than those of Schemes 3 and 6. Scheme 3 relies on the proximity auxiliary action voltage waveform of the SZ access SC, which is only slightly better than Scheme 6. However, in Figure 9b, the TZ1 voltage waveforms show that Schemes 2 and 3 are both significantly better than Scheme 6. The voltage fluctuation of the transient process in Scheme 3 is better than that of Scheme 2, though the difference is not substantial.

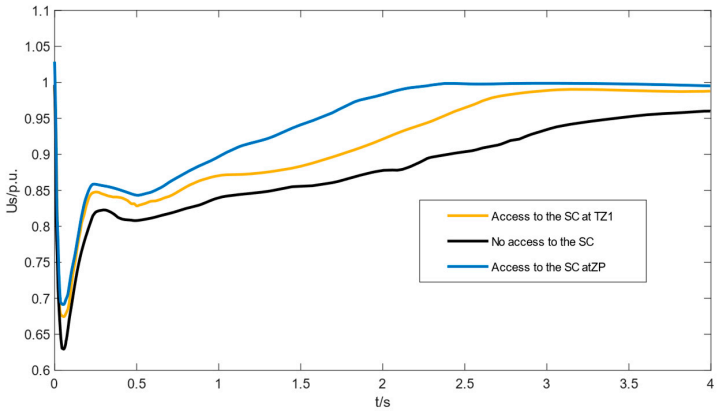


(**a**)

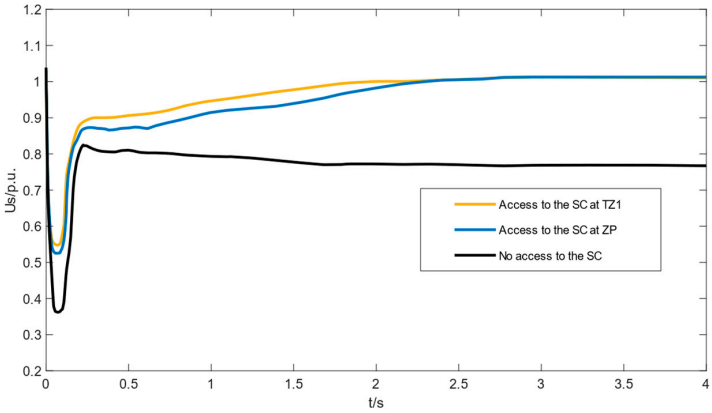
Figure 9. *Cont.*



(**b**)



(**c**)



(**d**)

Figure 9. Comparison of ZP and TZ1 transient voltage waveform under AC fault. (**a**) ZP node voltage at fault A. (**b**) TZ1 node voltage at fault A. (**c**) ZP node voltage at fault B. (**d**) TZ1 node voltage at fault B.

From Figure 9c,d, it can be observed that the voltage curves of both Scheme 2 and 3 are similar, and both can return to the pre-fault voltage level. In Figure 9d, the voltage fluctuation of Scheme 6, which is not connected to the SC, is larger and lower than the dynamic load critical stabilization voltage U_k due to successive phase change failures. This increases the induction motor slip, leading to motor blocking and triggering transient voltage instability. Additionally, a comparison between Schemes 2 and 3 reveals that when the SC is connected to ZP, the ZP voltage dips and recovery speeds are slightly better. Conversely, the TZ1 voltage waveform is slightly better. Therefore, from the perspective of

transient voltage stability of the overall system, Scheme 2 is superior to Scheme 3. Given that the economic costs of investment, operation, and maintenance are nearly the same, it is more reasonable to choose Scheme 2 with the optimal configuration of the SC.

5.3. Sensitivity Analysis of the SC Configuration Results in Multi-Feed DC Environment

In order to analyze the sensitivity of the large-capacity SC proposed under different dynamic load models, taking the SZ converter station and the JS UHV DC as examples, the three-phase short-circuit fault at 40% of the SZ–DW3 line is set to simulate and verify the capacity configuration of the SC under different working conditions in Table 7.

Table 7. The results of the capacity allocation under the dynamic load access ratio of 60–65%.

Dynamic Load Share	Critical Stabilization Voltage (p.u.)	Maximum Reactive Power Consumption of the Converter (MVar)	SC Accessed Capacity (MVar)	SC Accessed Number
60	0.51	984	600	2
61	0.54	922	600	2
62	0.57	1058	900	3
63	0.59	1101	900	3
64	0.61	1142	900	3
65	0.62	1286	900	3

As shown in Table 7, as the proportion of dynamic load access increases, the ability to maintain transient voltage stability deteriorates. Only by raising the critical stabilization voltage can the system voltage stability be preserved. Therefore, to meet the reactive power consumption of the converter, a larger capacity SC must be configured. Simulation verification of the SC capacity configuration is conducted under the condition of a 60% dynamic load access ratio. The DC system's reactive power output and demand, as well as dynamic load slip variation, are illustrated in Figure 10.

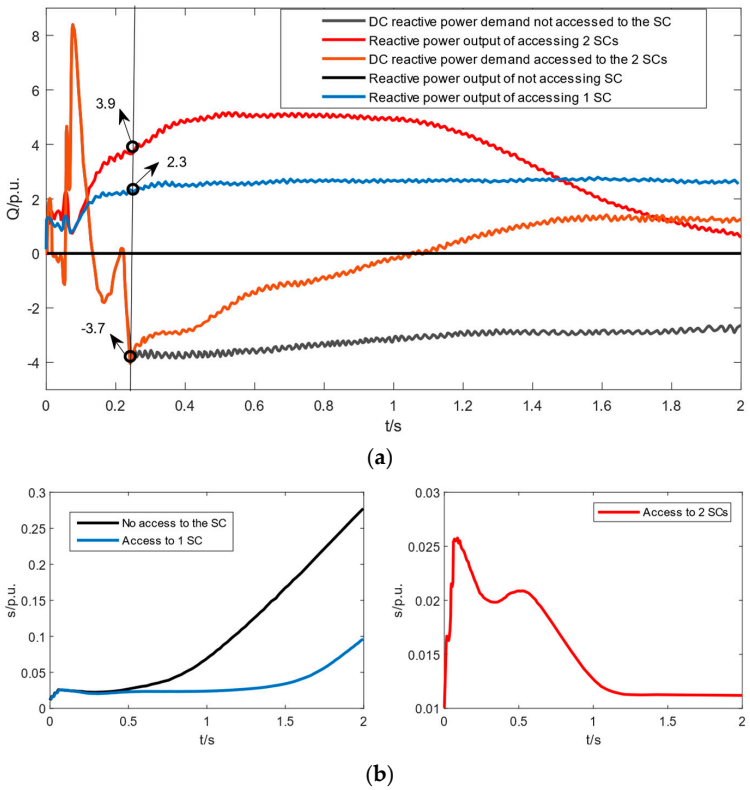


Figure 10. DC system reactive power output and demand, dynamic load slip variations. (**a**) Reactive power output and demand with different numbers of SC accessed. (**b**) Dynamic load slip variations with different numbers of SC accessed.

Without SC access, the reactive power demand cannot be met due to the failure of the DC continuous phase change, causing a continuous increase in dynamic load slip and resulting in system instability. After connecting the first SC, although the enhanced magnetic field achieves nearly 2.3 times of reactive power output, it still fails to satisfy the reactive power demand of the converter, which ultimately causes the bus voltage to drop to a critical level, resulting in the instability of the system. When two SCs are connected, the enhanced magnetic field increases the reactive power output to 3.9 times, which satisfies the reactive power demand of the converter. After fault removal, the slip gradually decreases to zero, and the system returns to its pre-fault state.

6. Conclusions and Future Work

6.1. Conclusions

The proposed optimal configuration model of the large-capacity SC under dynamic load critical stability constraints is verified in a multi-fed DC region. By analyzing the results, the following conclusions can be drawn:

1. The optimal configuration model for SCs in a multi-feeder DC environment is proposed. Results indicate that, compared to other schemes, Scheme 2 (1500 MVar) performs significantly better in terms of voltage dips and recovery speed, while the economic costs of investment (0.55 billion RMB), operation, and maintenance remain similar. The proposed optimal configuration model effectively addresses the lack of theoretical support for configuring large-capacity regulators in multi-feed-in DC areas;
2. The sub-transient and transient reactive power output characteristics of the SC are established. For the first time, the critical stable voltage index U_k for dynamic loads is defined, leading to the calculation of the specific reactive power compensation target of the regulator under varying dynamic load ratios. As the proportion of dynamic load access increases, the system's ability to maintain transient voltage stability deteriorates. Increasing the critical stability voltage is essential to maintaining system voltage stability. Therefore, based on Table 7, only a larger capacity regulator can be configured to meet the reactive power consumption of the converter;
3. This paper conducts qualitative and quantitative analyses of the DC reactive power and dynamic characteristics of induction motors following an AC system failure. The study reveals the impact of transient DC reactive power changes on the transient voltage stability mechanism of a multi-feed DC area with dynamic load access. Through comparative analysis, it is determined that the installation of a large-capacity regulator can effectively enhance the DC system voltage, thereby preventing system destabilization caused by the stalling of induction motors. Without SC access as shown in Figure 10, the reactive power demand cannot be met due to the failure of the DC continuous phase change, causing a continuous increase in dynamic load slip and resulting in system instability. After connecting the first SC, although the enhanced magnetic field achieves nearly 2.3 times of reactive power output, it still fails to satisfy the reactive power demand of the converter, which ultimately causes the bus voltage to drop to a critical level, resulting in the instability of the system. When two SCs are connected, the enhanced magnetic field increases the reactive power output to 3.9 times, which satisfies the reactive power demand of the converter. After fault removal, the slip gradually decreases to zero, and the system returns to its pre-fault state.

6.2. Limitations and Future Work

Currently, the SC optimal configuration of the UHV DC recipient grid is still undergoing continuous development. However, there are some limitations of the existing strategies, and future research can focus on the following aspects:

1. Future optimization models for SC configuration of the UHV DC recipient grid can consider integrating novel user-side behaviors [27] to enhance their applicability in various scenarios;

2. With the strategic objective of achieving 'carbon peak, carbon neutral', China will phase out low-efficiency and high-energy-consumption generators, while increasing the proportion of new energy output. Therefore, it is worth exploring a multi-stage DC carrying capacity assessment method for the receiving end grid in light of the gradual phasing out of conventional power sources and the construction timeline of UHV DC SC configuration projects [28].

Author Contributions: L.Z. conceptualized the idea of this research and carried out the theoretical analysis. Z.W. and Y.L. contributed to the design of the methodology and case study, and writing and revising the paper. Y.W. provided important comments on the structure and format of the paper. X.W. and H.Y. provided important comments on language and the data for the example. H.S. contributed to the writing and revising of the paper. All authors have read and agreed to the published version of the manuscript.

Funding: This work was supported by the State Grid Science and Technology Project (No. 5100-202356023A-1-1-ZN).

Data Availability Statement: The original contributions presented in the study are included in the article; further inquiries can be directed at the corresponding author.

Conflicts of Interest: Authors Lang Zhao, Zhidong Wang, Yizheng Li, and Xueying Wang were employed by the company State Grid Economic and Technological Research Institute Co., Ltd. Author Yao Wang was employed by Economic and Technological Research Institute of State Grid Shanxi Electric Power Co., Ltd. Author Haifeng Yu was employed by the Economic and Technological Research Institute of State Grid Hunan Electric Power Co., Ltd. The remaining author declares that the research was conducted in the absence of any commercial or financial relationships that could be construed as a potential conflict of interest.

Nomenclature

$Q_{ac\text{-}dc}$	reactive power exchange in the AC/DC hybrid system	$f_I()$	the low-voltage current-limiting control model
Q_{rpc}	reactive power provided by the SVC of the converter station	$Q_{inc,max}$	the maximum converter reactive power consumption
Q_{inc}	the reactive power consumed by a single six-pulse wave converter	Q_{SVC}	the rated reactive power output of the SVC installed in converter station i
n	the number of six-pulse wave converters	m_i and n_i	the number of SCs and converters installed in converter station i
U_d and I_d	the real-time voltage and current of the UHV DC system, respectively	Δu_s	the value of the bus voltage drop
X_c	the equivalent reactance of the converter	T	the control time constant of the excitation system
α, μ, and γ	the trigger angle, overlap angle, and turn-off angle of the converter, respectively	K_a	the strong excitation multiplier of the excitation system
U_{eq}	the equivalent AC power source	ΔE_f	the hypothetical no-load potential change
X_L	the equivalent reactance of the AC/DC interconnection	$C_{ta,i}$	the initial investment and installation cost of the SC at converter station i
U_s	the terminal voltage	C_m	the operation and maintenance cost per unit capacity of the SC
X_s, X_r, R_r, and s	the stator reactance, rotor reactance, rotor resistance, and slip of dynamic loads, respectively	Q_i	the capacity of the SC installed at converter station i
P_{dc} and Q_{dc}	the DC active and reactive power	λ_i	the transient voltage stability margin of converter station i
P_e	electromagnetic torque	U_{it}	the bus voltage at moment t of converter station i
S_{ac} and S_M	the AC system short-circuit capacity and dynamic load capacity, respectively	U_{ik}	the critical stabilization voltage of the bus at converter station i
Ω	the mechanical angular velocity of rotation	x	different configuration schemes of the SC
k_L	the loading rate of dynamic load	M	the solution set comprising all possible configuration schemes
a	the mechanical torque	f_1^* and f_2^*	the optimal solutions of individual sub-objective functions within the solution set M
Δi_d,	d-axis current variation	t_k	the fault removal time
X_d'' and T_d''	the d-axis sub-transient reactance and short-circuit time constant	T_J	the rotor inertia time constant
X_d' and T_d'	the d-axis transient reactance and short-circuit time constant	T_k and T_P	the mechanical torque and electromagnetic torque
T_a	the time constant of the non-periodic component of the stator		

References

1. Zhang, X.; Liu, F.; Wang, S. Measures to enhance new energy consumption in extra-high voltage direct current feeder grids. *Proc. CSU-EPSA* **2022**, *34*, 135–141.
2. Tang, G.; Pang, H.; He, Z. Development and application of advanced AC/DC power transmission technology in China. *Proc. CSEE* **2016**, *36*, 1760–1771. (In Chinese)
3. Li, P.; Zhou, H.; Yao, W.; Wang, L.; Yang, C.; Li, C.; Wen, J. A review on phase change failure of high-voltage direct current transmission systems in the context of multiple feed-in structures. *Power Grid Technol.* **2022**, *46*, 834–850.
4. Mazzanti, G.; Diban, B. The Effects of Transient Over-voltages on the Reliability of HVDC Extruded Cables. Part 1: Long Temporary Overvoltages. *IEEE Trans. Power Syst.* **2021**, *36*, 3784–3794. [CrossRef]
5. Jin, Y.; Yu, Z.; Li, M.; Jiang, W. Comparison of new generation regulator and power electronic reactive power compensation device applied in extra-high voltage AC and DC grids. *Power Grid Technol.* **2018**, *42*, 2095–2102.
6. Hadavi, S.; Saunderson, J.; Mehrizi-Sani, A.; Bahrani, B. A Planning Method for Synchronous Condensers in Weak Grids Using Semi-definite Optimization. *IEEE Trans. Power Syst.* **2023**, *38*, 1632–1641. [CrossRef]
7. Guo, Q.; Li, Z. A review on the development of synchronous regulator. *Proc. CSEE* **2023**, *43*, 6050–6064.
8. Zheng, C.; Sun, H.; Yang, D. Transient voltage instability criterion and control based on wide-area branch response. *Proc. CSEE* **2023**, *43*, 9470–9481.
9. Ma, W.; Wang, L.; Li, M.; Shin, X.; Wu, F.; Xu, Y. SLCC converter technology for ultra-high voltage direct current transmission in new power systems. *High Volt. Eng.* **2022**, *48*, 4941–4948.
10. Wang, Y.; Zhang, Y.; Zhou, Q. Research on the application of new generation large-capacity regulator in power grid. *Power Grid Technol.* **2017**, *41*, 22–28.
11. Yang, H.; Cai, Z.; Zhu, L. Dynamic characteristics of reactive power in DC system and its impact on transient voltage stability of the receiving end grid. *Electr. Power Autom. Equip.* **2017**, *37*, 86–92.
12. Xiao, F.; Wang, T.; Gao, Y. Research on reactive power compensation and fast response mechanism of regulator based on extra-high voltage AC/DC hybrid grid. *Power Syst. Prot. Control* **2019**, *47*, 93–100.
13. Sun, P.; Yao, W.; Huang, D. Technical and economic comparison between STATCOM and new type of regulator. *South. Power Grid Technol.* **2021**, *15*, 82–88.
14. Suo, Z.; Liu, J.; Jiang, W. Research on the configuration of regulator for large-scale new energy DC transmission system. *Electr. Power Autom. Equip.* **2019**, *39*, 124–129.
15. Chang, N.; Huo, C.; Liu, F. Research on optimal configuration of regulating camera for improving transient voltage stability level of weak feeder grid. *Power Syst. Prot. Control* **2019**, *47*, 90–95.
16. Wu, L.; Li, Y.; Yu, S. Stability analysis of wind power aggregation system based on short circuit ratio index. *Electr. Power Autom. Equip.* **2022**, *42*, 72–78.
17. Wang, Z.; Liu, M.; Li, H. Optimal allocation method of regulating camera to enhance new energy cluster delivery capacity of weak grid. *Electr. Power Autom. Equip.* **2024**, *44*, 30–36. [CrossRef]
18. Jiang, T.; Dong, Y.; Wang, C. Transient voltage stability assessment of the receiving end power system based on graph convolution and bi-directional long and short-term memory networks. *Power Grid Technol.* **2023**, *47*, 4937–4951.
19. Zhou, N.; Meng, Q.; Zhang, Y. Automatic optimal allocation of synchronous regulator capacity in DC receiving system. *Power Syst. Clean Energy* **2022**, *38*, 86–94.
20. Wang, Q.; Li, N.; Tang, X. Synchronous regulator camera placement method to cope with multi-feed-in DC phase change failure. *Power Syst. Autom.* **2019**, *43*, 222–227.
21. Zhou, Y.; Sun, H.; Xu, S.; Wang, X.; Zaho, B.; Zhu, Y. Synchronous condenser optimized configuration scheme for power grid voltage strength improvement. *Power Syst. Technol.* **2022**, *46*, 3848–3856. (In Chinese)
22. Mokhtari, M.; Gharehpetian, G.B. Integration of energy balance of soil ionization in cigre grounding electrode resistance model. *IEEE Trans. Electromagn. Compat.* **2018**, *60*, 402–413. [CrossRef]
23. Gu, X.; Bai, Y.; Li, S. Optimisation method for the recovery decision of AC/DC hybrid grid receiving end system considering wind power uncertainty. *Proc. CSEE* **2024**, 1–14. Available online: http://kns.cnki.net/kcms/detail/11.2107.TM.20240402.1052.010.html (accessed on 29 September 2024).
24. Li, Q.; Zhang, D.; Chen, M. Calculation method for high-frequency risk assessment of high-voltage flexible DC in multiple DC-fed transmission systems. *South. Power Grid Technol.* **2023**, *17*, 1–9.
25. Giannelos, S.; Borozan, S.; Aunedi, M.; Zhang, X.; Ameli, H.; Pudjianto, D.; Konstantelos, I.; Strbac, G. Modelling Smart Grid Technologies in Optimisation Problems for Electricity Grids. *Energies* **2023**, *16*, 5088. [CrossRef]
26. Zhang, Y.; Xu, Y.; Zhang, R.; Dong, Z.Y. A missing-data tolerant method for data-driven short-term voltage stability assessment of power systems. *IEEE Trans. Smart Grid* **2019**, *10*, 5663–5674. [CrossRef]

27. Chen, P.; Guan, L. Research on analysis and modelling of dynamic reactive power demand and its power recovery characteristics in DC transmission system. *Mod. Electr. Power* **2017**, *34*, 50–58.
28. Luo, Y.; Lu, C.; Zhu, L.; Song, J. Graph convolutional network-based interpretable machine learning scheme in smart grids. *IEEE Trans. Autom. Sci. Eng.* **2023**, *20*, 47–58. [CrossRef]

Disclaimer/Publisher's Note: The statements, opinions and data contained in all publications are solely those of the individual author(s) and contributor(s) and not of MDPI and/or the editor(s). MDPI and/or the editor(s) disclaim responsibility for any injury to people or property resulting from any ideas, methods, instructions or products referred to in the content.